

Excitation Frequency Dependence of Noise and Minimum Detectable Force in AM-AFM

Kenichi Umeda^{1,2} and Noriyuki Kodera¹

¹ *Nano Life Science Institute (WPI-NanoLSI),*

Kanazawa University, Kakuma-machi, Kanazawa, Ishikawa, 920-1192, Japan.

² *PRESTO/JST, 4-1-8 Honcho, Kawaguchi, Saitama 332-0012, Japan.*

Corresponding Authors

Dr. Kenichi Umeda (E-mail: umeda.k@staff.kanazawa-u.ac.jp)

Prof. Noriyuki Kodera (E-mail: nkodera@staff.kanazawa-u.ac.jp)

Abstract

Amplitude-modulation atomic force microscopy (AM-AFM) is a powerful tool for observing nanoscale surface structures with minimal disruption. As we discussed previously, AM-AFM maximizes detection sensitivity when exciting the cantilever at the resonance slope rather than the resonance frequency. Nevertheless, it remains unclear how AM noise depends on the excitation frequency or what the optimal excitation frequency is for the signal-to-noise ratio. Furthermore, no theoretical studies have investigated the noise bandwidth in the closed-loop system of AFM. Here, we formulate a quantitative theory of the minimum detectable force that accounts for the excitation frequency dependence. Our findings indicate that the AM noise dependence on excitation frequency can be approximated by a harmonic oscillator model when the oscillation amplitude exceeds the noise level. Under Brownian noise-limited conditions, the minimum detectable force decreases as the excitation frequency is lowered, approaching the dynamic-mode AFM limit.

1. Introduction

Amplitude-modulation (tapping-mode) atomic force microscopy (AM-AFM) is a powerful technique for visualizing the nanoscale topography of the sample surface [1-6]. With its ability to operate in both ambient and liquid environments, AM-AFM has significantly advanced research in fields such as electrochemistry, biology, and polymer science [3,7-12]. In particular, it has become essential in biological research due to its ability to observe under physiological conditions with very weak forces, especially minimal frictional forces [3,12,13]. The advancement of AM-AFM has also led to the development of high-speed AFM (HS-AFM), which enables video-rate imaging while maintaining low interaction forces [12,14,15]. However, to expand the applicability of this technique to highly fragile bioconjugates, which can be damaged by forces as low as a few pN, further force reduction is required.

Since the minimum detectable force (F_{\min}) is ultimately constrained by the signal-to-noise ratio (SNR), theoretical equations have been proposed since the invention of AFM [1,3,6,14,16-24]. As we have previously discussed [25,26], AM-AFM possesses a distinctive attribute wherein the force detection sensitivity is maximized when the cantilever is excited at the resonance slope rather than the resonance frequency (f_0), in contrast to other dynamic mode AFMs. However, exciting the cantilever at f_0 is still commonly utilized [9,27-29], as it is both experimentally and theoretically convenient for quantitative force estimation. Additionally, off-resonance excitation combined with peak force detection has recently been proposed to suppress dynamic impact forces [30].

Thus, despite the various excitation frequencies used in AM-AFM, no research has thoroughly discussed the optimal excitation frequency from the perspective of the SNR. In particular, no studies have examined whether AM noise depends on the excitation frequency or what theoretical framework governs it. Furthermore, to quantitatively estimate noise experimentally, it is necessary to

determine the equivalent noise bandwidth (ENBW) [31]. However, no studies have investigated the ENBW in the closed-loop system of AFM, possibly because many researchers approximately equate the measurement bandwidth with the ENBW.

In this study, we perform a comprehensive analysis of the cantilever's excitation frequency dependence of the SNR in AM-AFM. First, we derive an equation for the frequency dependence of the force gradient, following the approach in the previous study [25]. Next, through simulations, we demonstrate that the excitation frequency dependence of AM noise can be approximated using a simple harmonic oscillator (SHO) model. Finally, we develop a quantitative theory of F_{\min} in AM-AFM incorporating this excitation frequency dependence, which serves as a benchmark for the system.

2. Force Gradient Dependent on Driving Frequency

In AFM experiments, it is necessary to apply a force that exceeds the noise level at a minimum to enable the probe tip to approach the sample surface. Therefore, F_{\min} , defined as the reciprocal of the SNR, has been widely adopted as a metric for evaluating instrumental performance [1,3,6,14,16-24]. As previously studied [25,26], in AM-AFM, the tip-sample interaction force (F_{ts}) can be estimated from amplitude reduction based on a large-amplitude approximation. However, in contrast to static-mode AFM, dynamic-mode AFM is more likely to detect the resonance shift resulting from the force gradient ($F'_{ts} \equiv k_{ts}$), rather than the force itself. Consequently, theoretical equations for the minimum detectable force gradient ($k_{ts,\min}$) in a small-amplitude limit has been commonly utilized [13,20-24]. To facilitate comparison with other theories, we first derive an analytical solution for k_{ts} in AM-AFM.

As derived in previous studies [5,25], when the tip-sample interaction is small and the dissipation term can be neglected, G_{cl} , the transfer function of the cantilever based on a SHO model, is expressed by

$$G_{cl}(\tilde{\omega}_{\text{drive}}) = \frac{1}{k_{cl} \left(1 - \tilde{\omega}_{\text{drive}}^2 - \frac{2}{k_z A_{cl}^2} \langle F_{ts} \cdot z_{\text{tip}} \rangle \right) + i(\tilde{\omega}_{\text{drive}} / Q_{cl})}, \quad (1)$$

where k_{cl} , A_{cl} , Q_{cl} , and z_{tip} are the spring constant, oscillation amplitude, quality factor, and displacement of the cantilever, respectively. $\tilde{\omega}_{\text{drive}}$ is a normalized driving frequency (f_{drive}) that is defined as follows:

$$\tilde{\omega}_{\text{drive}} \equiv \frac{\omega_{\text{drive}}}{\omega_0} = \frac{f_{\text{drive}}}{f_0}, \quad (2)$$

Hereafter, we denote f and ω ($= 2\pi f$) as a certain frequency and its angular frequency, respectively.

The A_{cl} can be obtained by

$$A_{cl}(\tilde{\omega}_{drive}) = |G_{cl}(\tilde{\omega}_{drive})| F_{drive} = \frac{A_0}{\sqrt{\left(1 - \tilde{\omega}_{drive}^2 - \frac{2}{k_{cl} A_{cl}^2} \langle F_{ts} \cdot z_{tip} \rangle\right)^2 + (\tilde{\omega}_{drive} / Q_{cl})^2}}, \quad (3)$$

where F_{drive} is the driving force and A_0 represents A_{cl} at $\tilde{\omega}_{drive} = 0$. Furthermore, by using the free oscillation amplitude (A_{free}), A_{cl} can be expressed as follows:

$$A_{cl}(\tilde{\omega}_{drive}) = A_{free} \sqrt{\frac{(1 - \tilde{\omega}_{drive}^2)^2 + (\tilde{\omega}_{drive} / Q_{cl})^2}{\left(1 - \tilde{\omega}_{drive}^2 - \frac{2}{k_{cl} A_{cl}^2} \langle F_{ts} \cdot z_{tip} \rangle\right)^2 + (\tilde{\omega}_{drive} / Q_{cl})^2}}. \quad (4)$$

When A_{cl} is sufficiently small for k_{ts} to be considered linear during one period of oscillation, a small-amplitude approximation can be employed as follows:

$$\lim_{A_{free} \rightarrow 0} F_{ts} \approx \langle F_{ts} \rangle + k_{ts} A_{cl} \cos \omega_{drive} t. \quad (5)$$

Using this equation we obtain an approximation as follows [6]:

$$\lim_{A_{free} \rightarrow 0} \langle F_{ts} \cdot z_{tip} \rangle \approx \frac{k_{ts} A_{cl}^2}{2}. \quad (6)$$

Substituting this equation into Eq. (4) and solving for k_{ts} yields the following equation:

$$\lim_{A_{free} \rightarrow 0} k_{ts} = -\frac{k_{cl}}{\tilde{A}_{cl}} \left[-\left(1 - \tilde{\omega}_{drive}^2\right) \tilde{A}_{cl} \begin{matrix} \text{rep} \\ \text{att} \end{matrix} \pm \sqrt{\left(1 - \tilde{\omega}_{drive}^2\right)^2 + (\tilde{\omega}_{drive} / Q_{cl})^2} \left(1 - \tilde{A}_{cl}^2\right) \right], \quad (7)$$

where "rep" and "att" are denoted above and below the \pm symbol denote the repulsive ($\langle F_{ts} \rangle > 0$) and the attractive ($\langle F_{ts} \rangle < 0$) forces, respectively. This convention will be followed throughout the paper.

\tilde{A}_{cl} is a normalized A_{cl} that is defined as:

$$\tilde{A}_{cl} \equiv \frac{A_{cl}}{A_{free}} = \frac{A_{free} + \Delta A_{ts}}{A_{free}}, \quad (8)$$

where ΔA_{ts} is the amplitude change resulting from the tip-sample interaction. In the absence of feedback error, \tilde{A}_{cl} can be identified with the setpoint ratio. When excited at f_0 , the equation can be simplified to

$$\lim_{\tilde{A}_{cl} \rightarrow 0} k_{ts} = \mp \frac{k_{cl}}{Q_{cl}} \sqrt{\frac{1}{\tilde{A}_{cl}^2} - 1}. \quad (9)$$

First, we analyze the repulsive regime using calculations with typical HS-AFM parameters: $f_0 = 1$ MHz, $k_{cl} = 0.1$ N/m, and $Q_{cl} = 1.5$. In Fig. 1(a), the calculation of Eq. (7) indicates that k_{ts} increases as \tilde{A}_{cl} decreases. Notably, at $f_{drive} = f_0$, k_{ts} increases steeply, exhibiting nonlinear behavior near $\tilde{A}_{cl} = 1$. In contrast, the peak frequency (f_{peak}) is 0.88 MHz, and when f_{drive} is lowered below this value, the rise of k_{ts} near $\tilde{A}_{cl} = 1$ becomes linear. These features are strikingly similar to the average force observed in a previous study [25]. However, for $\tilde{A}_{cl} < 0.5$, unlike the average force, k_{ts} does not saturate and instead diverged infinitely as \tilde{A}_{cl} decreases. Thus, it is evident that when f_{drive} is below f_{peak} , a linear approximation can be made at $\tilde{A}_{cl} \sim 1$, similar to the average force.

For the attractive regime, the calculations are performed using typical ambient AM-AFM parameters: $f_0 = 1$ MHz, $k_{cl} = 3$ N/m, and $Q_{cl} = 300$. In Fig. 1(b), similar to the repulsive regime, near $\tilde{A}_{cl} = 1$, k_{ts} increases steeply at $f_{drive} = f_0$, while the slope approaches linearity at the resonance slope frequencies, referred to as UMF and UMS, which will be defined later. Conversely, as f_{drive} rises beyond the resonance slope frequencies, the increase in k_{ts} becomes steeper.

Therefore, similar to $\langle F_{ts} \rangle$, we found that, when excited at the resonance slope frequency, the k_{ts} slope can be accurately represented by a linear approximation as follows:

$$\frac{\partial k_{ts}}{\partial \tilde{A}_{cl}} = \pm \frac{k_{cl}}{\tilde{A}_{cl}^2 Q_{cl}} \frac{\tilde{\omega}_{drive}^2 + Q_{cl}^2 (1 - \tilde{\omega}_{drive}^2)^2}{\sqrt{(1 - \tilde{A}_{cl}^2) \tilde{\omega}_{drive}^2 + Q_{cl}^2 (1 - \tilde{\omega}_{drive}^2)^2}}, \quad (10)$$

where the upper and lower signs correspond to the repulsive and attractive regimes, respectively. By taking the limit of $\tilde{A}_{cl} \rightarrow 1$, we obtain

$$\lim_{\tilde{A}_{cl} \rightarrow 1} \frac{\partial k_{ts}}{\partial \tilde{A}_{cl}} = \frac{k_{cl}}{Q_{cl}} \left[\frac{\tilde{\omega}_{drive}^2}{Q_{cl} (1 - \tilde{\omega}_{drive}^2)} + Q_{cl} (1 - \tilde{\omega}_{drive}^2) \right] (\tilde{\omega}_{drive} \neq 1). \quad (11)$$

Therefore, when ΔA_{ts} is sufficiently small, k_{ts} can be linearly approximated as follows:

$$k_{ts} \approx \beta_{\Delta A \rightarrow k} \Delta A_{ts}, \quad (12)$$

where $\beta_{\Delta A \rightarrow k}$, which represents the conversion coefficient from ΔA_{ts} to k_{ts} , is obtained as follows:

$$\begin{aligned} \beta_{\Delta A \rightarrow k} &\equiv \frac{1}{A_{\text{free}}} \lim_{\tilde{A}_{\text{cl}} \rightarrow 1} \frac{\partial k_{ts}}{\partial \tilde{A}_{\text{cl}}} \\ &= \frac{1}{A_{\text{free}}} \frac{k_{\text{cl}}}{Q_{\text{cl}}} \left[\frac{\tilde{\omega}_{\text{drive}}^2}{Q_{\text{cl}}(1-\tilde{\omega}_{\text{drive}}^2)} + Q_{\text{cl}}(1-\tilde{\omega}_{\text{drive}}^2) \right] \quad (\tilde{\omega}_{\text{drive}} \neq 1). \end{aligned} \quad (13)$$

Meanwhile, according to the previous study [25], the equation for $\langle F_{ts} \rangle$ is expressed as follows:

$$\langle F_{ts} \rangle = \frac{k_{\text{cl}} A_{\text{free}}}{2} \left[-(1-\tilde{\omega}_{\text{drive}}^2) \tilde{A}_{\text{cl}} \begin{matrix} \text{rep} \\ \pm \\ \text{att} \end{matrix} \sqrt{(1-\tilde{\omega}_{\text{drive}}^2)^2 + (\tilde{\omega}_{\text{drive}} / Q_{\text{cl}})^2 (1-\tilde{A}_{\text{cl}}^2)} \right], \quad (14)$$

When excited at the resonance slope, we can use the linear approximation as follows:

$$\langle F_{ts} \rangle \approx \alpha_{\Delta A \rightarrow F} \Delta A_{ts}, \quad (15)$$

where $\alpha_{\Delta A \rightarrow F}$ represents the conversion coefficient from ΔA_{ts} to $\langle F_{ts} \rangle$, which is expressed by

$$\alpha_{\Delta A \rightarrow F} = -\frac{k_{\text{cl}}}{2Q_{\text{cl}}} \left[\frac{\tilde{\omega}_{\text{drive}}^2}{Q_{\text{cl}}(1-\tilde{\omega}_{\text{drive}}^2)} + Q_{\text{cl}}(1-\tilde{\omega}_{\text{drive}}^2) \right] \quad (\tilde{\omega}_{\text{drive}} \neq 1). \quad (16)$$

Eqs. (13) and (16) are valid for $\tilde{\omega}_{\text{drive}} < 1$ and $\tilde{\omega}_{\text{drive}} > 1$ in the repulsive and attractive regimes, respectively. In Fig. 1(c,d), the calculation of Eq. (13) shows k_{ts} as a function of $\tilde{\omega}_{\text{drive}}$, with a form consistent with the corresponding data for $\langle F_{ts} \rangle$ [25], and thus, Eq. (13) shares an identical form as Eq. (16), differing only in the coefficients.

As with $\langle F_{ts} \rangle$, by solving $\partial \beta_{\Delta A \rightarrow k} / \partial \tilde{\omega}_{\text{drive}} = 0$, the lower and upper MinForce frequencies (f_{LMF} and f_{UMF}) are obtained as follows (see the arrows):

$$\tilde{\omega}_{\text{LMF}} \equiv \frac{f_{\text{LMF}}}{f_0} = \sqrt{1 - \frac{1}{Q_{\text{cl}}}} \quad (Q_{\text{cl}} \geq 1), \quad (17)$$

$$\tilde{\omega}_{\text{UMF}} \equiv \frac{f_{\text{UMF}}}{f_0} = \sqrt{1 + \frac{1}{Q_{\text{cl}}}}. \quad (18)$$

Consequently, by exciting at the MinForce frequencies, both the sensitivities of $\langle F_{\text{ts}} \rangle$ and k_{ts} can be maximized. By substituting these equations into Eqs. (12) and (13), a straightforward analytical solution for k_{ts} at f_{LMF} and f_{UMF} can be derived as follows:

$$k_{\text{ts}}|_{\text{LMF}} \approx \frac{k_{\text{cl}}}{Q_{\text{cl}}} \left(2 - \frac{1}{Q_{\text{cl}}} \right) \frac{\Delta A_{\text{ts}}}{A_{\text{free}}} \quad (Q_{\text{cl}} \geq 1) \quad \text{if } \langle F_{\text{ts}} \rangle > 0, \quad (19)$$

$$k_{\text{ts}}|_{\text{UMF}} \approx -\frac{k_{\text{cl}}}{Q_{\text{cl}}} \left(2 + \frac{1}{Q_{\text{cl}}} \right) \frac{\Delta A_{\text{ts}}}{A_{\text{free}}} \quad \text{if } \langle F_{\text{ts}} \rangle < 0. \quad (20)$$

The equation derived here will be used to derive the equation for SNR in Section 8.

3. AM Noise at Resonance Frequency in AM-AFM

In this section, we proceed to derive the quantitative equation for AM noise in AM-AFM. Among the various noise sources, the thermal Brownian noise of the cantilever becomes dominant in state-of-the-art AFM instruments [32,33], including HS-AFM systems [34-36], due to the optimization of the optical beam deflection (OBD) system. Consequently, the effect of other noises is not considered in the present theory. Initially, an equation for the AM noise when excited at f_0 is derived, following past studies [1,6]. The displacement of the cantilever, based on the SHO model, due to thermal noise $\langle z_{\text{th}}^2 \rangle$ is given by the equipartition theorem as follows:

$$\frac{1}{2}k_{\text{cl}}\langle z_{\text{th}}^2 \rangle = \frac{1}{2}k_{\text{B}}T, \quad (21)$$

where k_{B} and T are the Boltzmann constant and system temperature, respectively. By coupling this equation with G_{cl} , the Brownian noise spectral density in the cantilever (n_{th}) can be obtained as follows [16,37,38]:

$$n_{\text{th}}(\omega_{\text{drive}}) = |G_{\text{cl}}(\omega_{\text{drive}})|F_{\text{th}}, \quad (22)$$

where the thermal force F_{th} is expressed by

$$F_{\text{th}} = \sqrt{\frac{4k_{\text{cl}}k_{\text{B}}T}{Q_{\text{cl}}\omega_0}}. \quad (23)$$

Therefore, we obtain the common expression of n_{th} as follows:

$$n_{\text{th}}(\omega_{\text{drive}}) = \sqrt{\frac{4k_{\text{B}}T}{\omega_0 k_{\text{cl}} Q_{\text{cl}}} \frac{1}{[(1 - \tilde{\omega}_{\text{drive}}^2)]^2 + (\tilde{\omega}_{\text{drive}} / Q_{\text{cl}})^2}}. \quad (24)$$

By approximating G_{cl} by a Taylor polynomial near f_0 and imposing the condition $Q_{\text{cl}} \gg 1$, it can be approximated by the transfer function of first-order lag as follows [37,38]:

$$G_{cl}(\omega_{drive}) \Big|_{\omega_{drive} \rightarrow \omega_0} \approx \frac{1}{k_{cl}} \frac{-iQ_{cl}}{1 + i(\omega_m / \omega_{cl})}, \quad (25)$$

$$\omega_m = \omega_{drive} - \omega_0,$$

where ω_{cl} is the radial bandwidth of the cantilever expressed by

$$\omega_{cl} = \frac{\omega_0}{2Q_{cl}}. \quad (26)$$

Using this equation, n_{th} near f_0 can be calculated as follows [37,38]:

$$n_{th} \Big|_{approx}(\omega_{drive}) = \sqrt{\frac{4k_B T Q_{cl}}{k_{cl} \omega_0} \frac{1}{1 + (\omega_m / \omega_{cl})^2}}. \quad (27)$$

The AM noise is obtained by integrating the noise spectral density over the upper and lower sidebands as follows:

$$N_{th}^{AM} = \sqrt{\int_{-B_{ENBW}}^{B_{ENBW}} (n_{th}(f_0 + f_m))^2 df_m} \quad (28)$$

$$= \sqrt{\frac{4k_B T Q_{cl}}{k_{cl} \omega_0} 2f_c \left[\tan^{-1}(f_m / f_{cl}) \right]_0^{B_{ENBW}}},$$

where B_{ENBW} represents ENBW. The relationship $\omega_{cl} > 2\pi B_{ENBW}$ always holds because the bandwidth of the entire closed-loop includes all components in addition to the cantilever. Therefore, this equation can be approximated by

$$N_{th}^{AM} \approx \sqrt{\frac{4k_B T Q_{cl}}{k_{cl} \omega_0} (2B_{ENBW})}. \quad (29)$$

This equation was first derived in the early stages of AM-AFM development [2]. Unlike the original study, a factor of $\sqrt{2}$ is included here to account for two sidebands, as also mentioned in a recent study [6].

4. AM Noise at Arbitrary Driving Frequencies in AM-AFM

We next consider the dependence of the AM noise on f_{drive} , the characteristics of which remain unknown. Due to the difficulty of analytically calculating the noise characteristics, simulations were performed with a time interval of 10 ns, corresponding to a sampling frequency of 100 MHz (Fig. 2(a)). Initially, Gaussian noise was superimposed on the drive signal. Subsequently, fast Fourier transform (FFT) was performed to convert the time-domain signal into the frequency domain, and the noise spectrum was generated by multiplying it with the transfer function of the first eigenmode of the cantilever. To consider the bandwidth of the OBD sensor, the transfer function of a first-order low-pass filter (LPF) with a cutoff frequency of 5 MHz was also multiplied. The frequency-domain signal was then converted back into the time domain via an inverse FFT, followed by amplitude detector processing to calculate an amplitude signal. Finally, an FFT was performed again to convert the signal into the frequency domain, generating the AM noise spectrum.

The transfer function of amplitude detector must also be considered when estimating the AM noise. Simulations were performed with a Fourier-analysis-based (FAB) algorithm, which is commonly used in employed in HS-AFM setups [39] and operates on principle analogous to that of the lock-in amplifier, commonly used in standard AM-AFM instruments (Fig. 2(b)). In this algorithm, the deflection signal is separately multiplied by the cosine and sine components, and after integration, the Root-Sum-of-Squares (RSS) value is calculated to produce the amplitude signal. The integrator circuit can be replaced by an LPF. The transfer function of the FAB in the time domain is expressed as the convolution integral of the instantaneous amplitude and an impulsive response of the detector f_{det} as follows:

$$A_{\text{AM}}^{\text{FAB}}(t) = \int_{-\infty}^{\infty} A_{\text{AM}}(t-\tau) f_{\text{det}}(\tau) d\tau, \quad (30)$$

where f_{det} is expressed as a rectangular function with an integral time ΔT_{integ} as follows:

$$f_{\text{det}}(t) = \begin{cases} \frac{1}{\Delta T_{\text{integ}}} & 0 \leq t < \Delta T_{\text{integ}} \\ 0 & \text{elsewhere} \end{cases}, \quad (31)$$

$$\Delta T_{\text{integ}} = \frac{2n_{\text{integ}}\pi}{\omega_{\text{drive}}}, \quad (32)$$

where n_{integ} is the integration number of the cantilever oscillation period. By performing a Fourier transform, Eq. (30) can be converted in the frequency domain using a cross correlation as follows:

$$\hat{A}_{\text{AM}}^{\text{FAB}}(i\omega_{\text{AM}}) = \hat{A}_{\text{AM}}(i\omega_{\text{AM}})\hat{f}_{\text{det}}(i\omega_{\text{AM}}), \quad (33)$$

where \hat{x} represents the Fourier transform of x . The Fourier transform of f_{det} is expressed as

$$\begin{aligned} \hat{f}_{\text{det}}(i\omega_{\text{AM}}) &= \int_{-\infty}^{\infty} f_{\text{det}}(t) \exp(-i\omega_{\text{AM}}t) dt \\ &= \frac{1 - \exp(-i\Delta T_{\text{integ}}\omega_{\text{AM}})}{i\Delta T_{\text{integ}}\omega_{\text{AM}}}, \end{aligned} \quad (34)$$

where the absolute value can be expressed as a sinc function, as follows:

$$\left| \hat{f}_{\text{det}}(\omega_{\text{AM}}) \right| = \left| \text{sinc} \left(\frac{\Delta T_{\text{integ}}\omega_{\text{AM}}}{2} \right) \right|, \quad (35)$$

We performed simulations with a common HS-AFM experimental parameters: $k_{\text{cl}} = 0.1$ N/m, $f_0 = 1$ MHz, and $T = 298$ K. The data presented in each spectrum result from 400 integrations. In Fig. 2(c,d), as theoretically predicted, the simulated spectra exhibit the characteristics of a sinc function, with a constant noise level at low frequencies. Furthermore, the cutoff frequency tends to be reduced to lower frequencies concurrently with increasing n_{integ} . However, in contrast to $Q_{\text{cl}} = 1.5$, no significant change was observed for $Q_{\text{cl}} = 10$. To examine this further, the AM response of the cantilever is plotted (yellow broken curves) expressed by

$$n_{\text{th}}^{\text{AM}}(\tilde{\omega}_{\text{drive}} = 1, \omega_{\text{AM}}) = \sqrt{\frac{4k_{\text{B}}TQ_{\text{cl}}}{k_{\text{cl}}\omega_0} \frac{2}{1 + (\omega_{\text{AM}}/\omega_{\text{cl}})^2}}. \quad (36)$$

The data demonstrate that for $Q_{\text{cl}} = 1.5$, the actual bandwidth is less than that of the cantilever, indicating that the amplitude detector limits the total bandwidth. Conversely, for $Q_{\text{cl}} = 10$, no notable

discrepancy is observed, suggesting that the cantilever's bandwidth is the predominant limiting factor.

We next examine the AM noise spectra with varying f_{drive} from 0.5–1.5 MHz. Although the excitation efficiency changes depending on f_{drive} , simulations were performed while adjusting the excitation power to maintain a constant amplitude value across all f_{drive} . In Fig. 2(e,f), the noise level is predominantly consistent at low frequencies but exhibits a gradual decline at higher frequencies for f_{drive} values of 0.5–1 MHz. It is also evident that the noise level at low frequency varies depending on f_{drive} , peaking at $f_{\text{drive}} = f_0$. This trend is more pronounced for $Q_{\text{cl}} = 10$ than for $Q_{\text{cl}} = 1.5$, suggesting that the noise level can be reduced by exciting at a frequency other than f_0 . However, at $f_{\text{drive}} = 1.5$ MHz, a gain noise peak appears in the high frequency range (indicated by the arrow), which may pose to a risk of feedback oscillation.

To quantitatively examine the f_{drive} dependence of the AM noise density, the average noise density in the low-frequency range was quantified using approximately 100 integrated spectra, as depicted in Fig. 2(a). In Fig. 3(a,b), we first investigate the A_{cl} dependence. When excited at $A_{\text{cl}} = 1 \text{ nm}_{\text{p-0}}$ or higher, the results for both $Q_{\text{cl}} = 1.5$ and $Q_{\text{cl}} = 10$ match the SHO approximation as follows:

$$n_{\text{th}}^{\text{AM}}(\tilde{\omega}_{\text{drive}}, \omega_{\text{AM}} = 0) = \sqrt{\frac{4k_{\text{B}}TQ_{\text{cl}}}{\omega_0 k_{\text{cl}}} \frac{2}{[Q_{\text{cl}}(1 - \tilde{\omega}_{\text{drive}}^2)]^2 + \tilde{\omega}_{\text{drive}}^2}}, \quad (37)$$

where the factor of $\sqrt{2}$ is included to account for the two sidebands. However, when A_{cl} is smaller than $1 \text{ nm}_{\text{p-0}}$, reducing A_{cl} causes the noise levels near the resonance peak to decrease, while those outside the peak increase. Consequently, the peak shape gradually flattens, and at $A_{\text{cl}} = 0 \text{ nm}$, the peak noise is reduced to about half. The amplitude criterion at which the noise spectrum deviates from that of SHO was found to be independent of Q_{cl} but proportional to the root-mean-square (RMS) noise, which can be obtained from Eq. (21) as follows:

$$\sqrt{\langle z_{\text{th}}^2 \rangle} = \sqrt{\frac{k_{\text{B}}T}{k_{\text{cl}}}}. \quad (38)$$

By substituting the simulation parameter $k_{cl} = 0.1$ N/m, the RMS noise is calculated to be 0.2 nm. Thus, by comparing $A_{cl} = 1$ nm_{p-0}, we found that the criterion amplitude ($A_{criteria}$) is approximately five times the RMS noise, as follows:

$$A_{criteria} \approx 5\sqrt{\langle z_{th}^2 \rangle}. \quad (39)$$

In AM-AFM measurements, excitation is typically performed at A_{cl} values that are more than ten times the RMS noise, indicating that the SHO approximation is applicable in most cases. Therefore, we found that the AM noise account for $\tilde{\omega}_{drive}$ can be obtained as follows:

$$N_{th}^{AM} \Big|^{accur} \approx \sqrt{\frac{4k_B T Q_{cl} (2B_{ENBW})}{k_{cl} \omega_0 \left[Q_{cl} (1 - \tilde{\omega}_{drive}^2) \right]^2 + \tilde{\omega}_{drive}^2}}. \quad (40)$$

To gain a more comprehensive understanding, we further investigate the cause of the non-ideal noise characteristics at excessively low amplitudes. We performed simulations based on the output of the cosine integral, bypassing the RSS calculation in the FAB. In Fig. 3(c,d), the results perfectly match the SHO model, even when the drive amplitude is zero. This finding indicates that this phenomenon arises from the coupling of high-frequency and low-frequency noises due to the RSS calculation, which occurs only when the noise level becomes comparable to A_{cl} .

We also examined the n_{integ} dependence of the noise spectra (Fig. 3(e,f)). With excitation at $A_{cl} = 0.3$ nm_{p-0}, n_{integ} was varied from 1 to 8, and the results asymptotically approached the SHO model as n_{integ} increases. For $Q_{cl} = 1.5$, results matched the SHO model at $n_{integ} = 8$. For $Q_{cl} = 10$, the SHO model was not achieved until $n_{integ} = 32$. This result implies that, even if A_{cl} falls below the noise criterion, reducing the bandwidth of the amplitude detector can suppress the coupling.

6. Conversion Factors for Noise Bandwidth

To simply calculate the noise level, we have defined B_{ENBW} as the bandwidth, which represents the cutoff frequency of an ideal brick-wall filter. However, B_{FB45° is typically employed for the feedback bandwidth calculation [14], which necessitates the derivation of an expression for converting B_{FB45° to B_{ENBW} . Therefore, we examine the characteristics of the closed-loop transfer function (G_{FB}). As shown in the block diagram in Fig. 4(a), the feedback loop of AM-AFM functions to make the difference between the tip trajectory and the surface topography zero [4]. Therefore, if the change in surface topography is the input signal and the tip trajectory is the output signal, G_{FB} is expressed as follows:

$$G_{\text{FB}}(\omega_{\text{FB}}) = \frac{G_{\text{cl}}^{\text{AM}}(\omega_{\text{FB}})G_{\text{amp}}(\omega_{\text{FB}})G_{\text{PID}}(\omega_{\text{FB}})G_z(\omega_{\text{FB}})}{1 + G_{\text{cl}}^{\text{AM}}(\omega_{\text{FB}})G_{\text{amp}}(\omega_{\text{FB}})G_{\text{PID}}(\omega_{\text{FB}})G_z(\omega_{\text{FB}})}, \quad (41)$$

where $G_{\text{cl}}^{\text{AM}}$ and G_{amp} represent the transfer functions of the AM detection of the cantilever and amplitude detector, respectively, expressed as follows:

$$G_{\text{cl}}^{\text{AM}}(\omega) = \frac{1}{1 + i\omega / \omega_{\text{cl}}}, \quad (42)$$

$$G_{\text{amp}}(\omega) = \exp(-i\omega\Delta\tau_{\text{amp}}). \quad (43)$$

where $\Delta\tau_{\text{amp}}$ is the dead time of the amplitude detector, given as follows:

$$\Delta\tau_{\text{amp}} = -\frac{\phi_{\text{amp}}}{\omega_{\text{drive}}}, \quad (44)$$

where ϕ_{amp} represents the constant phase lag relative to the cantilever's oscillation cycle, specific to the type of amplitude detector used.

G_{PID} represents the transfer functions of the proportional–integral–derivative (PID) controller, expressed as follows:

$$G_{\text{PID}}(\omega) = \frac{K_p}{1+i\omega/\omega_p} + \frac{K_i}{i\omega} + \frac{iK_d\omega}{1+i\omega/\omega_d}. \quad (45)$$

where K_p , K_i and K_d are the proportional, integral, and derivative gains, respectively, and ω_p and ω_d are the radial cutoff frequencies of proportional and derivative gains, respectively. As in the actual experiment, the PID gain should be optimized to maximize the measurement bandwidth while preventing feedback oscillations. The derivative gain is commonly avoided because it amplifies high-frequency noise and higher-order vibration modes, often resulting in unstable feedback. Similarly, the effect of the proportional gain is often limited compared to integral gain due to similar reasons. Therefore, in this simulation, only the integral gain was considered.

G_z represents the transfer function of Z-scanner, expressed as follows:

$$G_z(\omega) = \frac{Q_z}{Q_z \left[1 - (\omega/\omega_z)^2 \right] + i(\omega/\omega_z)}. \quad (46)$$

where ω_p and Q_z are the radial resonance frequency and quality factor of the Z-scanner, respectively. In some AM-AFM systems, particularly in HS-AFM, the signal is displayed through a mock Z-scanner circuit. However, it does not affect the transfer function of the tip trajectory, as it is not part of the closed loop.

We conducted a simulation using typical HS-AFM parameters: $f_0 = 1.2$ MHz, $Q_{\text{cl}} = 1.5$, $f_z = 150$ kHz, $Q_z = 0.7$, and $\phi_{\text{amp}} = 90^\circ$. The simulation results are presented in Fig. 4(b,c), showing a steep decline in both gain and phase with increasing feedback frequency, resembling a fourth-order lag LPF. To derive an analytical solution, a theoretical equation that can be solved without simulations is necessary. Thus, we fitted the result using a two-stage cascade Sallen-Key (fourth-order lag) transfer function (G_{SK}), which is expressed as follows:

$$G_{\text{FB4th}}(\tilde{\omega}_{\text{FB4th}}) \approx (G_{\text{SK}}(\tilde{\omega}_{\text{FB4th}}))^2 = \frac{1}{\left[\left(1 - \tilde{\omega}_{\text{FB4th}}^2 \right) + i(\tilde{\omega}_{\text{FB4th}}/Q_{\text{SK}}) \right]^2}, \quad (47)$$

where Q_{SK} represents the Q-factor of the individual Sallen-Key filter. $\tilde{\omega}_{FB4th}$ represents a normalized feedback frequency, defined as follows:

$$\tilde{\omega}_{FB4th} \equiv \frac{\omega_{FB}}{2\pi B_{FB180^\circ}}, \quad (48)$$

where B_{FB180° represents the cutoff frequency at which the phase lag in the feedback signal respect to the surface topography becomes -180° (Fig. 4(c)). Note that the individual Sallen-Key transfer function is identical to that of SHO (Eq. (1) with $\langle F_{ts} \cdot z_{tip} \rangle = 0$); therefore, the magnitude and phase (ϕ_{FB}) of G_{FB} are expressed by

$$|G_{FB4th}(\tilde{\omega}_{FB4th})| \approx \frac{1}{(1 - \tilde{\omega}_{FB4th}^2)^2 + (\tilde{\omega}_{FB4th}/Q_{SK})^2}, \quad (49)$$

$$\phi_{FB4th} = \angle G_{FB4th}(\tilde{\omega}_{FB4th}) = 2 \tan^{-1} \left(-\frac{\tilde{\omega}_{FB4th}}{Q_{SK}} \frac{1}{1 - \tilde{\omega}_{FB4th}^2} \right), \quad (50)$$

In Fig. 4(b,c), the simulation results were well fitted with a cascade of two-stage Sallen-Key filter, with a parameter of $Q_{SK} = 0.68$, and $B_{FB180^\circ} = 115$ kHz. This fitting is due to the cantilever and PID functioning as a first-order lag system, while the Z-scanner acts as a second-order lag system, resulting in an overall fourth-order lag system.

To convert B_{FB45° to B_{ENBW} , it is necessary to convert to B_{FB180° first, then to B_{ENBW} as follows:

$$B_{FB180^\circ} = \alpha_{45^\circ \rightarrow 180^\circ} B_{FB45^\circ}, \quad (51)$$

$$B_{ENBW} = \alpha_{180^\circ \rightarrow ENBW} B_{FB180^\circ}, \quad (52)$$

where $\alpha_{45^\circ \rightarrow 180^\circ}$ and $\alpha_{180^\circ \rightarrow ENBW}$ represent the conversion factor from B_{FB45° to B_{FB180° and from B_{FB180° to B_{ENBW} , respectively (Fig. 4(d)). Substituting $\phi_{FB4th} = -\pi/4$ and Eq. (51) into Eq. (50) and solving the equation for $\alpha_{45^\circ \rightarrow 180^\circ}$ gives

$$\alpha_{45^\circ \rightarrow 180^\circ} = \frac{2Q_{SK}(\sqrt{2}-1)}{-1 + \sqrt{[2Q_{SK}(\sqrt{2}-1)]^2 + 1}}. \quad (53)$$

As shown in Fig. 4(b), to obtain B_{ENBW} , we need to find the frequency where the area of the rectangular region (indicated by the green broken line) matches the integral of the power of the Sallen-Key cascade over all frequencies. Since the power of the Sallen-Key cascade has a second-order pole, performing a contour integral using the residue theorem gives $\alpha_{180^\circ \rightarrow \text{ENBW}}$ as follows:

$$\begin{aligned}\alpha_{180^\circ \rightarrow \text{ENBW}} &= \frac{1}{2\pi} \int_0^\infty \frac{1}{\left[\left(1 - \tilde{\omega}_{\text{FB4th}}^2\right)^2 + \left(\tilde{\omega}_{\text{FB4th}}/Q_{\text{SK}}\right)^2 \right]^2} d\omega_{\text{FB}} \\ &= \frac{\pi}{4} Q_{\text{SK}} (Q_{\text{SK}}^2 + 1).\end{aligned}\quad (54)$$

Therefore, by combining these two equations, we can directly convert from B_{FB45° to B_{ENBW} as follows:

$$B_{\text{ENBW}} = \alpha_{45^\circ \rightarrow \text{ENBW}} B_{\text{FB45}^\circ}, \quad (55)$$

where $\alpha_{45^\circ \rightarrow \text{ENBW}}$ represent the conversion factor from B_{FB45° to B_{ENBW} (Fig. 4(d)). This expression is obtained as follows:

$$\begin{aligned}\alpha_{45^\circ \rightarrow \text{ENBW}} &= \alpha_{180^\circ \rightarrow \text{ENBW}} \cdot \alpha_{45^\circ \rightarrow 180^\circ} \\ &= \frac{\pi}{4} Q_{\text{SK}} (Q_{\text{SK}}^2 + 1) \frac{2Q_{\text{SK}} (\sqrt{2} - 1)}{-1 + \sqrt{\left[2Q_{\text{SK}} (\sqrt{2} - 1)\right]^2 + 1}}.\end{aligned}\quad (56)$$

In Fig. 4(e), the calculation of these factors reveals that, with increasing Q_{SK} , $\alpha_{45^\circ \rightarrow 180^\circ}$ decreases whereas $\alpha_{180^\circ \rightarrow \text{ENBW}}$ and $\alpha_{45^\circ \rightarrow \text{ENBW}}$ increase. By assuming that a typical value of $Q_{\text{SK}} = 0.7$, we found that $\alpha_{45^\circ \rightarrow \text{ENBW}}$ can be approximated by

$$\alpha_{45^\circ \rightarrow \text{ENBW}} \approx 3. \quad (57)$$

We then examine ambient AM-AFM experiments, where the bandwidth of the cantilever is generally the rate-limiting factor due to the high Q_{cl} . For example, a simulation was performed under the following typical parameters: $f_0 = 1.2$ MHz, $Q_{\text{cl}} = 300$, $f_Z = 50$ kHz, $Q_Z = 10$, and $\phi_{\text{amp}} = 360^\circ$. In Fig. 4(f,g), both the gain and phase curves can be well-fitted with a single Sallen-Key filter, whose

transfer function is given as follows:

$$G_{\text{FB2nd}}(\tilde{\omega}_{\text{FB2nd}}) \approx G_{\text{SK}}(\tilde{\omega}_{\text{FB2nd}}) = \frac{1}{(1 - \tilde{\omega}_{\text{FB2nd}}^2) + i(\tilde{\omega}_{\text{FB2nd}}/Q_{\text{SK}})}, \quad (58)$$

where $\tilde{\omega}_{\text{FB2nd}}$ represents a normalized feedback frequency, defined as follows:

$$\tilde{\omega}_{\text{FB2nd}} \equiv \frac{\omega_{\text{FB}}}{2\pi B_{\text{FB90}^\circ}}, \quad (59)$$

This means that, since the latency of the Z -scanner can be negligible, it can be expressed as a second-order lag system. Therefore, the conversion formula for the ENBW in a second-order lag system is derived below.

To convert B_{FB45° to B_{ENBW} , it is necessary to first convert B_{FB45° to B_{FB90° , then to B_{ENBW} as follows:

$$B_{\text{FB90}^\circ} = \beta_{45^\circ \rightarrow 90^\circ} B_{\text{FB45}^\circ}, \quad (60)$$

$$B_{\text{ENBW}} = \beta_{90^\circ \rightarrow \text{ENBW}} B_{\text{FB90}^\circ}, \quad (61)$$

where $\beta_{45^\circ \rightarrow 90^\circ}$ and $\beta_{90^\circ \rightarrow \text{ENBW}}$ represent the conversion factor from B_{FB45° to B_{FB180° and from B_{FB180° to B_{ENBW} , respectively (Fig. 4(h)). By performing the same calculation as for the fourth-order lag system, they can be obtained as follows.

$$\beta_{45^\circ \rightarrow 90^\circ} = \frac{2Q_{\text{SK}}}{-1 + \sqrt{(2Q_{\text{SK}})^2 + 1}}. \quad (62)$$

$$\beta_{90^\circ \rightarrow \text{ENBW}} = \frac{\pi}{2} Q_{\text{SK}}. \quad (63)$$

Therefore, we can directly convert from B_{FB45° to B_{ENBW} as follows:

$$B_{\text{ENBW}} = \beta_{45^\circ \rightarrow \text{ENBW}} B_{\text{FB45}^\circ}, \quad (64)$$

where $\beta_{45^\circ \rightarrow \text{ENBW}}$ represent the conversion factor from B_{FB45° to B_{ENBW} (Fig. 4(h)), obtained as follows:

$$\begin{aligned}
\beta_{45^\circ \rightarrow \text{ENBW}} &= \beta_{90^\circ \rightarrow \text{ENBW}} \cdot \beta_{45^\circ \rightarrow 90^\circ} \\
&= \frac{\pi}{2} Q_{\text{SK}} \frac{2Q_{\text{SK}}}{-1 + \sqrt{(2Q_{\text{SK}})^2 + 1}}.
\end{aligned} \tag{65}$$

We plot these factors in Fig. 4(i), revealing that, as Q_{SK} increases, $\beta_{45^\circ \rightarrow 90^\circ}$ decreases, while $\beta_{90^\circ \rightarrow \text{ENBW}}$ and $\beta_{45^\circ \rightarrow \text{ENBW}}$ increase. Although the trends are similar to those of a fourth-order system, the overall coefficients are found to be low. Assuming $Q_{\text{SK}} = 0.7$, we found that $\beta_{45^\circ \rightarrow \text{ENBW}}$ can be approximated by

$$\beta_{45^\circ \rightarrow \text{ENBW}} \approx 2.1. \tag{66}$$

To summarize the results above, the conversion factor varies depending on the system but generally falls within the range of 2 to 3. Therefore, for fourth-order and second-order lag systems, N_{th} can be directly calculated from $B_{\text{FB}45^\circ}$ by applying the conversion factors to Eq. (40), as follows:

$$N_{\text{th}}^{\text{AM}} \Big|_{4\text{th}}^{\text{accur}} = \sqrt{\frac{4k_{\text{B}} T Q_{\text{cl}}}{\omega_0 k_{\text{cl}}} \frac{(6B_{\text{FB}45^\circ})}{Q_{\text{cl}}^2 (1 - \tilde{\omega}_{\text{drive}}^2)^2 + \tilde{\omega}_{\text{drive}}^2}}, \tag{67}$$

$$N_{\text{th}}^{\text{AM}} \Big|_{2\text{nd}}^{\text{accur}} = \sqrt{\frac{4k_{\text{B}} T Q_{\text{cl}}}{\omega_0 k_{\text{cl}}} \frac{(4.2B_{\text{FB}45^\circ})}{Q_{\text{cl}}^2 (1 - \tilde{\omega}_{\text{drive}}^2)^2 + \tilde{\omega}_{\text{drive}}^2}}. \tag{68}$$

7. Minimum Detectable Force in AM-AFM from Previous Studies

Before the derivation of $k_{ts,min}$ for AM-AFM ($k_{ts,min}^{AM}$), we examine the theories of dynamic-mode AFM reported in previous literatures. In addition to AM-AFM, there are also frequency-modulation AFM (FM-AFM) [16] and phase-modulation AFM (PM-AFM) [17-19] as dynamic-mode AFMs.

The theoretical $k_{ts,min}$ for FM-AFM was first derived by Albrecht et al. ($k_{ts,min}^{FM}$) [16] as follows:

$$\lim_{A_{free} \rightarrow 0} k_{ts,min}^{FM} = \frac{rep}{att} \frac{1}{A_{free}} \sqrt{\frac{8k_{cl}k_B T}{Q_{cl}\omega_0} B_{ENBW}} = \frac{rep}{att} \sqrt{\frac{4k_{cl}k_B T}{Q_{cl}\omega_0 \langle z_{free}^2 \rangle}} B_{ENBW}. \quad (69)$$

where unlike the original literature, signs are included in the equation. $\sqrt{\langle z_{free}^2 \rangle}$ represents the RMS of z_{tip} under the free oscillation condition, which can be converted from A_{free} as follows:

$$\sqrt{\langle z_{free}^2 \rangle} = \frac{A_{free}}{\sqrt{2}}. \quad (70)$$

For PM-AFM, Fukuma et al. derived the equation below [17]:

$$\lim_{A_{free} \rightarrow 0} F_c |_{min}^{PM} = \frac{rep}{att} \sqrt{\frac{8k_{cl}k_B T}{Q_{cl}\omega_0} B_{ENBW}}. \quad (71)$$

According to the original literature, F_c is a Virial force defined as follows:

$$F_c = \frac{2}{A_{free}} \langle F_{ts} \cdot z_{tip} \rangle. \quad (72)$$

Therefore, by applying the small amplitude approximation of Eq. (6), we obtain $k_{ts,min}$ for PM-AFM

($k_{ts,min}^{PM}$) as follows:

$$\lim_{A_{free} \rightarrow 0} k_{ts,min}^{PM} = \frac{rep}{att} \frac{1}{A_{free}} \sqrt{\frac{8k_{cl}k_B T}{Q_{cl}\omega_0} B_{ENBW}} = \lim_{A_{free} \rightarrow 0} k_{ts,min}^{FM}. \quad (73)$$

As evident, $k_{ts,min}^{PM}$ is found to be equivalent to $k_{ts,min}^{FM}$, indicating that Eqs. (69) and (73) represent the

theoretical limit of dynamic-mode AFM.

The theoretical $k_{ts,\min}^{\text{AM}}$ when excited at f_0 was derived by McClelland et al. as follows [2]:

$$\lim_{A_{\text{free}} \rightarrow 0} k_{ts,\min}^{\text{AM}} \Big|_{\text{McClelland}} = \frac{\text{rep}}{\text{att}} \frac{1}{A_s} \sqrt{\frac{4k_{\text{cl}}k_{\text{B}}T}{Q_{\text{cl}}\omega_0}} (2B_{\text{ENBW}}) = \lim_{A_{\text{free}} \rightarrow 0} k_{ts,\min}^{\text{FM}}, \quad (74)$$

where A_s and z_s represent the oscillation amplitude and displacement of the sample, respectively, due to the authors' use of the sample-excitation system. In this equation, unlike in the original literature, a factor of $\sqrt{2}$ is included to account for the two sidebands. This adjustment renders the theoretical equation for AM-AFM and FM-AFM equivalent. However, this theoretical equation cannot be applied to most current AM-AFM systems, as they utilize a cantilever-excitation system.

Moreover, the theoretical $k_{ts,\min}^{\text{AM}}$ with the cantilever-excitation system when excited at MaxSlope derived by Martin et al. is expressed as follows [1]:

$$\begin{aligned} \lim_{Q_{\text{cl}} \rightarrow \infty} \left(\lim_{A_{\text{free}} \rightarrow 0} k_{ts,\min}^{\text{AM}} \right) \Big|_{\text{Martin}} &= \frac{\text{rep}}{\text{att}} \frac{1}{A_{\text{free}}} \sqrt{\frac{27k_{\text{cl}}k_{\text{B}}T}{Q_{\text{cl}}\omega_0}} (2B_{\text{ENBW}}) \\ &= \frac{3\sqrt{3}}{2} \lim_{A_{\text{free}} \rightarrow 0} k_{ts,\min}^{\text{FM}} \approx 2.60 \lim_{A_{\text{free}} \rightarrow 0} k_{ts,\min}^{\text{FM}}. \end{aligned} \quad (75)$$

Unlike the original equation, we account for the factor of $\sqrt{2}$. However, this equation is also not applicable to the liquid AM-AFM systems, as it is derived under the high Q_{cl} approximation. Additionally, while the conservative forces contribute a decrease in the excitation efficiency and frequency shifts [25], this equation only accounts for the frequency shift.

8. Minimum Detectable Force in AM-AFM vs. Driving Frequency

Using the equations formulated above, we next derive a more quantitative expression for F_{\min} , applicable to AM-AFM in any environment based on the linear approximation. Since F_{\min} can be obtained by setting $\Delta A = N_{\text{th}}$ [1,2], substituting the accurate noise equation (Eq. (40)), which rigorously accounts for the f_{drive} dependency, into Eqs. (12,13) and (15,16) yields

$$\lim_{A_{\text{free}} \rightarrow 0} k_{\text{ts,min}}^{\text{AM}} \Big|_{\text{accur}} = \begin{matrix} \text{rep} \\ \text{att} \end{matrix} \frac{1}{A_{\text{free}}} \sqrt{\frac{4k_{\text{cl}}k_{\text{B}}T}{\omega_0 Q_{\text{cl}}} \left\{ 1 + \left[\frac{\tilde{\omega}_{\text{drive}}}{Q_{\text{cl}}(1 - \tilde{\omega}_{\text{drive}}^2)} \right]^2 \right\}} (2B_{\text{ENBW}}) \quad (\tilde{\omega}_{\text{drive}} \neq 1), \quad (76)$$

$$\lim_{A_{\text{free}} \rightarrow \infty} \langle F_{\text{ts}} \rangle_{\text{min}}^{\text{AM}} \Big|_{\text{accur}} = \begin{matrix} \text{rep} \\ \text{att} \end{matrix} \sqrt{\frac{k_{\text{cl}}k_{\text{B}}T}{\omega_0 Q_{\text{cl}}} \left\{ 1 + \left[\frac{\tilde{\omega}_{\text{drive}}}{Q_{\text{cl}}(1 - \tilde{\omega}_{\text{drive}}^2)} \right]^2 \right\}} (2B_{\text{ENBW}}) \quad (\tilde{\omega}_{\text{drive}} \neq 1). \quad (77)$$

These equations are valid for $\tilde{\omega}_{\text{drive}} < 1$ and $\tilde{\omega}_{\text{drive}} > 1$ in the repulsive and attractive regimes, respectively. As is evident, $k_{\text{ts,min}}^{\text{AM}}$ has the same form as $\langle F_{\text{ts}} \rangle_{\text{min}}^{\text{AM}}$ with only different coefficients as follows:

$$\lim_{A_{\text{free}} \rightarrow \infty} \langle F_{\text{ts}} \rangle_{\text{min}}^{\text{AM}} \Big|_{\text{accur}} = \begin{matrix} \text{rep} \\ \text{att} \end{matrix} \frac{2}{A_{\text{free}}} \lim_{A_{\text{free}} \rightarrow 0} k_{\text{ts,min}}^{\text{AM}} \Big|_{\text{accur}}. \quad (78)$$

In Fig. 5(a,b), we examine the $\tilde{\omega}_{\text{drive}}$ dependence of $k_{\text{ts,min}}^{\text{AM}}$ or $\langle F_{\text{ts}} \rangle_{\text{min}}^{\text{AM}}$ normalized by their dynamic-mode limits. In the repulsive regime, $k_{\text{ts,min}}^{\text{AM}}$ decreases monotonically as $\tilde{\omega}_{\text{drive}}$ decreases, whereas in the attractive regime, $k_{\text{ts,min}}^{\text{AM}}$ decreases monotonically as $\tilde{\omega}_{\text{drive}}$ increases. This result indicates that, under ideal conditions, the maximum SNR in the repulsive regime is achieved at $\tilde{\omega}_{\text{drive}} = 0$, whereas in the attractive regime, it is achieved as $\tilde{\omega}_{\text{drive}}$ approaches infinity. Therefore, to examine the theoretical limit of $k_{\text{ts,min}}^{\text{AM}}$, we substitute $\tilde{\omega}_{\text{drive}} = 0$ into Eq. (76) and obtained the

following equation:

$$\lim_{A_{\text{free}} \rightarrow 0} k_{\text{ts,min}}^{\text{AM}} \Big|_{\tilde{\omega} \rightarrow 0}^{\text{accur}} = \lim_{A_{\text{free}} \rightarrow 0} k_{\text{ts,min}}^{\text{FM}}, \quad (79)$$

which is identical to the theoretical limit of dynamic-mode AFM (Eqs. (69) and (73)), thereby confirming the validity of the theoretical formulations presented in both the current and previous studies.

However, in practical experiments, the tip scanning introduces an additional force resulting from the feedback error, particularly when f_{drive} is misaligned with the resonance slope [26]. Moreover, $B_{\text{FB}45^\circ}$ deteriorates as f_{drive} declines, further amplifying the feedback error. Even without tip scanning, SNR is degraded by deflection signal fluctuations in the OBD system at low frequencies. As clearly seen in Fig. 5(a,b), both $k_{\text{ts,min}}$ and $\langle F_{\text{ts}} \rangle_{\text{min}}$ exhibit only slight reduction below the lower MinForce frequencies or above the upper MinForce frequencies (indicated by the arrows). Consequently, if scanning effect is taken into consideration, it is optimal to excite at the MinForce frequency, where the sensitivity of the AM signal is at its maximum. However, as the peak force detection method can be combined with off-resonance excitation [30], it may offer the potential for achieving a higher SNR.

Since $\tilde{\omega}_{\text{drive}}$ that can be used in practical AM-AFM experiments limited, we next analyze the Q_{cl} dependence of F_{min} when excited at the characteristic frequencies. By substituting Eqs. (17) and (18) into Eq. (76), simplified analytical expressions of $k_{\text{ts,min}}^{\text{AM}}$ for the lower and upper MinForce frequencies can be obtained as follows:

$$\lim_{A_{\text{free}} \rightarrow 0} k_{\text{ts,min}}^{\text{AM}} \Big|_{\text{LMF}}^{\text{accur}} = -\frac{1}{A_{\text{free}}} \sqrt{\frac{4k_{\text{cl}}k_{\text{B}}T}{\omega_0 Q_{\text{cl}}} \left(2 - \frac{1}{Q_{\text{cl}}}\right) (2B_{\text{ENBW}})} \quad (Q_{\text{cl}} \geq 1), \quad (80)$$

$$\lim_{A_{\text{free}} \rightarrow 0} k_{\text{ts,min}}^{\text{AM}} \Big|_{\text{UMF}}^{\text{accur}} = \frac{1}{A_{\text{free}}} \sqrt{\frac{4k_{\text{cl}}k_{\text{B}}T}{\omega_0 Q_{\text{cl}}} \left(2 + \frac{1}{Q_{\text{cl}}}\right) (2B_{\text{ENBW}})}. \quad (81)$$

Similarly, substituting Eqs. (17) and (18) into Eq. (77) gives simplified analytical equations for

$\langle F_{ts} \rangle_{\min}^{\text{AM}}$ as follows:

$$\lim_{A_{\text{free}} \rightarrow \infty} \langle F_{ts} \rangle_{\min}^{\text{AM}} \Big|_{\text{LMF}}^{\text{accur}} = \sqrt{\frac{k_{\text{cl}} k_{\text{B}} T}{\omega_0 Q_{\text{cl}}} \left(2 - \frac{1}{Q_{\text{cl}}} \right) (2B_{\text{ENBW}})} \quad (Q_{\text{cl}} \geq 1), \quad (82)$$

$$\lim_{A_{\text{free}} \rightarrow \infty} \langle F_{ts} \rangle_{\min}^{\text{AM}} \Big|_{\text{UMF}}^{\text{accur}} = -\sqrt{\frac{k_{\text{cl}} k_{\text{B}} T}{\omega_0 Q_{\text{cl}}} \left(2 + \frac{1}{Q_{\text{cl}}} \right) (2B_{\text{ENBW}})}, \quad (83)$$

To validate the derived equation, a calculation was performed using typical HS-AFM experimental conditions: $k_{\text{cl}} = 0.1$ N/m, $f_0 = 1$ MHz, $Q_{\text{cl}} = 1.5$, and $B_{\text{FB}45^\circ} = 25$ kHz, resulting in $\langle F_{ts} \rangle_{\min}^{\text{AM}} \Big|_{\text{LMF}} = 3.0$ pN. Since biomolecular imaging is typically conducted at around 10 pN, this value is highly realistic.

We next compare the Q_{cl} dependence of $k_{\text{ts},\min}$ derived in this study with those in the previous literatures [1,16]. To facilitate this comparison, these values, normalized by the dynamic-mode limit, are plotted in Fig. 5(c). As a result, $k_{\text{ts},\min}^{\text{AM}} \Big|_{\text{Martin}}$ systematically overestimates all other results across the entire Q_{cl} range, particularly under low Q_{cl} conditions. Furthermore, $k_{\text{ts},\min}^{\text{AM}}$ is higher than $k_{\text{ts},\min}^{\text{FM}}$ across the entire Q_{cl} range, especially under high Q_{cl} conditions, confirming that FM-AFM has an advantage over AM-AFM under vacuum conditions. To quantitatively estimate the difference, we take the limit as Q_{cl} approaches infinity in Eqs. (80) and (81), revealing that the expression for the lower and upper MinForce asymptotically approach an identical form, differing only by their signs, as follows:

$$\lim_{Q_{\text{cl}} \rightarrow \infty} \left(\lim_{A_{\text{free}} \rightarrow 0} k_{\text{ts},\min}^{\text{AM}} \Big|_{\text{MF}}^{\text{accur}} \right) = \sqrt{2} \lim_{A_{\text{free}} \rightarrow \infty} k_{\text{ts},\min}^{\text{FM}} \approx 1.41 \lim_{A_{\text{free}} \rightarrow \infty} k_{\text{ts},\min}^{\text{FM}}. \quad (84)$$

Therefore, we found that the SNR of AM-AFM is $\sqrt{2}$ times lower than that of FM-AFM in a high Q_{cl} environment, possibly because the detection sensitivity of k_{ts} is maximized at f_0 . In contrast, as Q_{cl} decreases, the SNR asymptotically approaches 1, becoming identical to that of FM-AFM. This result indicates that, under HS-AFM measurement conditions where Q_{cl} is 1.5 or less, measurements

can be performed with a minimum detection force sensitivity approaching the theoretical limit.

Furthermore, for comparison, we also examine the characteristics of the MaxSlope frequency, defined as the frequency at which the amplitude slope reaches its maximum. Similar to MinForce, there are both lower and upper MaxSlope frequencies, with analytical approximations derived in a previous study [25]. In Fig. 5(c), we found that the results are slightly higher than those of MinForce but exhibit a similar dependency on Q_{cl} . Taking the limit as Q_{cl} approaches infinity, we found that the expressions of the lower and upper MaxSlope frequencies asymptotically approach an identical form, differing only in sign, as follows:

$$\lim_{Q_{cl} \rightarrow \infty} \left(\lim_{A_{free} \rightarrow 0} k_{ts,min}^{AM} \right) \Big|_{MS}^{accur} = \sqrt{3} \lim_{A_{free} \rightarrow \infty} k_{ts,min}^{FM} \approx 1.73 \lim_{A_{free} \rightarrow \infty} k_{ts,min}^{FM}. \quad (85)$$

A previously study demonstrated that the detection sensitivity of MinForce is higher than that of MaxSlope by only 3% [25]; in contrast, we found that the difference becomes increased to 22% ($=\sqrt{3/2}-1$) in terms of SNR.

Finally, we compare F_{min} between static-mode and dynamic-mode AFM. The noise equation for static-mode AFM can be derived by integrating the Brownian noise density in the low-frequency range over the bandwidth, as follows:

$$N_{th}^{static} = \sqrt{\frac{4k_B T}{\omega_0 k_{cl} Q_{cl}}} B_{ENBW}. \quad (86)$$

Coupling this equation with Hooke's law yields F_{min} for the static mode as follows:

$$F_{min}^{static} = k_{cl} N_{th}^{static} = \sqrt{\frac{4k_{cl} k_B T}{\omega_0 Q_{cl}}} B_{ENBW}. \quad (87)$$

Meanwhile, to compare with the theoretical limit of $\langle F_{ts} \rangle_{min}^{AM}$, substituting $Q_{cl} = 1$ into Eq. (82) yields the equation as follows:

$$\lim_{A_{free} \rightarrow \infty} \langle F_{ts} \rangle_{min}^{AM} \Big|_{LMF}^{accur} (Q_{cl} = 1) = \sqrt{\frac{k_{cl} k_B T}{\omega_0 Q_{cl}}} (2B_{ENBW}) = \frac{1}{\sqrt{2}} F_{min}^{static}. \quad (88)$$

This equation indicates that the force sensitivity of AM-AFM is $\sqrt{2}$ times higher than static-mode AFM. This difference arises from the AM-AFM equation, which expresses the RMS force. Therefore, to convert the RMS force to the peak force, it is necessary to multiply by $\sqrt{2}$, assuming a linear force gradient. The results presented above also demonstrate that our derived theories are consistent with the theoretical formula for static-mode AFM.

9. Nonlinear Solutions for Minimum Detectable Force in AM-AFM

The theory described in the previous section relies on a linear approximation under idealized conditions. However, in practice, $k_{ts,\min}^{\text{AM}}$ and $\langle F_{ts} \rangle_{\min}^{\text{AM}}$ cannot be determined when the noise level exceeds A_{free} . To evaluate the applicability of the linear approximation, calculations were performed using the original nonlinear expressions in Eqs. (7) and (14) combined with Eq. (40). We calculated the Q_{cl} dependence of $k_{ts,\min}^{\text{AM}}$ and $\langle F_{ts} \rangle_{\min}^{\text{AM}}$ for various values of $A_{\text{free}}\sqrt{k_{\text{cl}}} \equiv Ak^{1/2}$, as the analytical results indicate that the curve shape varies with it. Similar to Fig. 5(c), both are normalized by the dynamic-mode limit. For $\langle F_{ts} \rangle_{\min}^{\text{AM}}$, since Eqs. (76) and (77) share the same form except for their coefficients, its dynamic-mode limit was assumed based on Eq. (69) as follows:

$$\lim_{A_{\text{free}} \rightarrow 0} \langle F_{ts} \rangle_{\min}^{\text{FM}} = \pm \frac{\text{rep}}{\text{att}} \sqrt{\frac{2k_{\text{cl}}k_{\text{B}}T}{Q_{\text{cl}}\omega_0}} B_{\text{ENBW}}. \quad (89)$$

Hereafter, $k_{ts,\min}^{\text{AM}}$ and $\langle F_{ts} \rangle_{\min}^{\text{AM}}$ are collectively referred to as F_{\min} . In Fig. 6(a,b), the calculation results for f_{LMF} and f_{UMF} show that when Q_{cl} is 4 or lower, both the nonlinear solutions are asymptotically close to the linear solution. However, as Q_{cl} increases, F_{\min} dissociates from the linear solution, that is, $k_{ts,\min}^{\text{AM}}$ diverges infinitely, while $\langle F_{ts} \rangle_{\min}^{\text{AM}}$ steeply decreases, indicating that the noise level exceeds A_{free} . Meanwhile, as $Ak^{1/2}$ increases, the nonlinear solutions approach the linear solution more closely. To achieve higher $Ak^{1/2}$, increasing k_{cl} is essential, as the validity of the linear k_{ts} approximation diminishes as A_{free} increases. In other words, a larger k_{cl} helps minimize the reduction in A_{cl} , even when the same force is applied. Typically, since sufficiently large A_{free} is employed relative to the noise level, the linear solution is expected to provide a good approximation across all Q_{cl} values.

Furthermore, F_{\min} at f_{peak} , where the linear approximations of Eqs. (76) and (77) are not valid, is

also analyzed in Fig. 6(c). The expression of f_{peak} is obtained as follows [25]:

$$\tilde{\omega}_{\text{peak}} \equiv \frac{\omega_{\text{peak}}}{\omega_0} = \frac{f_{\text{peak}}}{f_0} = \sqrt{1 - \frac{1}{2Q_{\text{cl}}^2}} \quad \left(Q_{\text{cl}} > \frac{1}{\sqrt{2}} \right). \quad (90)$$

The results exhibit a trend similar to that observed for f_{LMF} . Specifically, as Q_{cl} increases, $k_{\text{ts,min}}^{\text{AM}}$ tends to increase, and after reaching a plateau or peak, it rises again, while $\langle F_{\text{ts}} \rangle_{\text{min}}^{\text{AM}}$ tends to decrease after initially reaching a plateau or peak. Meanwhile, as $Ak^{1/2}$ increases, the prominence of the plateau increases and forms a peak, while the entire curve shifts to higher Q_{cl} values. This result indicates that, unlike f_{LMF} and f_{UMF} , F_{min} at f_{peak} cannot be represented by a simple analytical solution due to the dependence of the noise curves on experimental conditions. Similar to f_{LMF} and f_{UMF} , it becomes experimentally impractical in high Q_{cl} regions, where F_{min} diverges, as the magnitudes of the noise and A_{sp} become comparable. Therefore, only F_{min} in the plateau or peak regions are realistically meaningful and estimated to be at least three times greater than the dynamic-mode limit.

We also calculated F_{min} at f_0 in Fig. 6(d), which revealed a trend similar to f_{UMF} ; specifically, as Q_{cl} increases, both F_{min} decrease, but only $k_{\text{ts,min}}^{\text{AM}}$ diverges infinitely after reaching a minimum. However, at low Q_{cl} , a significant increase in F_{min} is observed at f_0 compared to f_{UMF} . Since only the low Q_{cl} region, where $k_{\text{ts,min}}^{\text{AM}}$ and $\langle F_{\text{ts}} \rangle_{\text{min}}^{\text{AM}}$ match each other, is experimentally meaningful, in this region, F_{min} is at least five times larger than the dynamic-mode limit and becomes even larger as Q_{cl} decreases or $Ak^{1/2}$ increases. Therefore, it was found that F_{min} at f_{peak} and f_0 are several times worse compared to those at f_{LMF} and f_{UMF} . However, this data suggests that at f_{peak} and f_0 , F_{min} can be reduced by keeping A_{sp} and k_{cl} as low as possible within the range where noise does not exceed A_{sp} .

10. Conclusions

In this study, we successfully derived theoretical equations for F_{\min} in AM-AFM, depending on the excitation frequency of the cantilever. Although the characteristics of AM noise vary slightly depending on the cantilever's oscillation amplitude, we found that it can be approximated by the SHO model, especially near the resonance peak when the amplitude is not excessively small. As the excitation frequency decreases, both force detection sensitivity and AM noise diminish, causing F_{\min} to approach the theoretical limit of dynamic-mode AFM. However, in practical experiments, it is advantageous to excite at the resonance slope frequency for minimizing feedback-induced forces. Under these conditions, lower Q_{cl} values bring the system closer to this theoretical limit. The theory derived here offers a benchmark for evaluating the absolute performance of instruments, particularly for observing fragile molecules and soft materials.

Figures

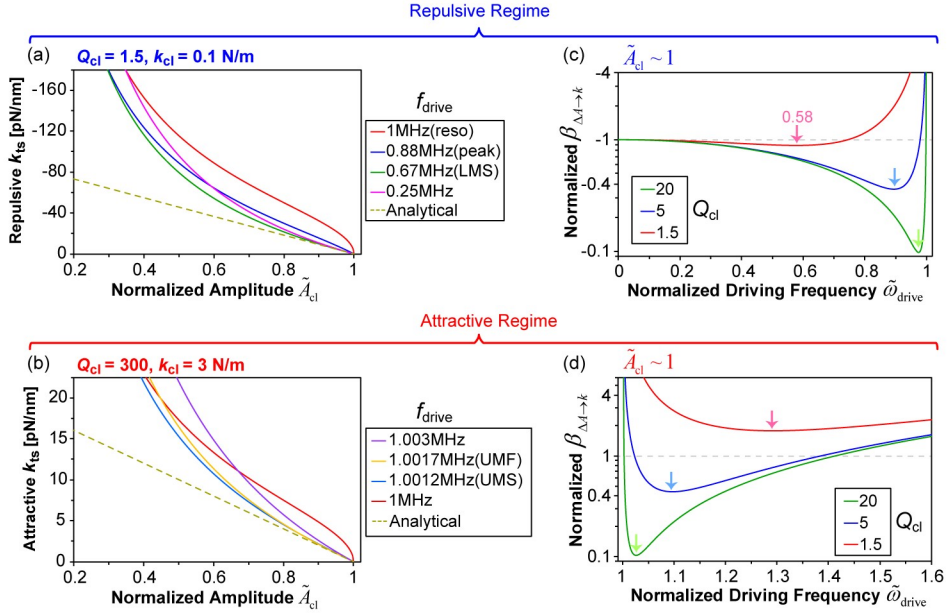


FIG. 1. (a,b) Normalized amplitude dependence of the force gradient at different driving frequencies in the repulsive (a) and attractive (b) regimes (Eq. (7)). (c,d) Driving frequency dependence of $\beta_{\Delta A \rightarrow F}$ ($\tilde{A}_{cl} = 1$) normalized by those at $f_{drive} = 0$ Hz for various Q_{cl} in the repulsive (c) and attractive (d) regimes (Eq. (13)).

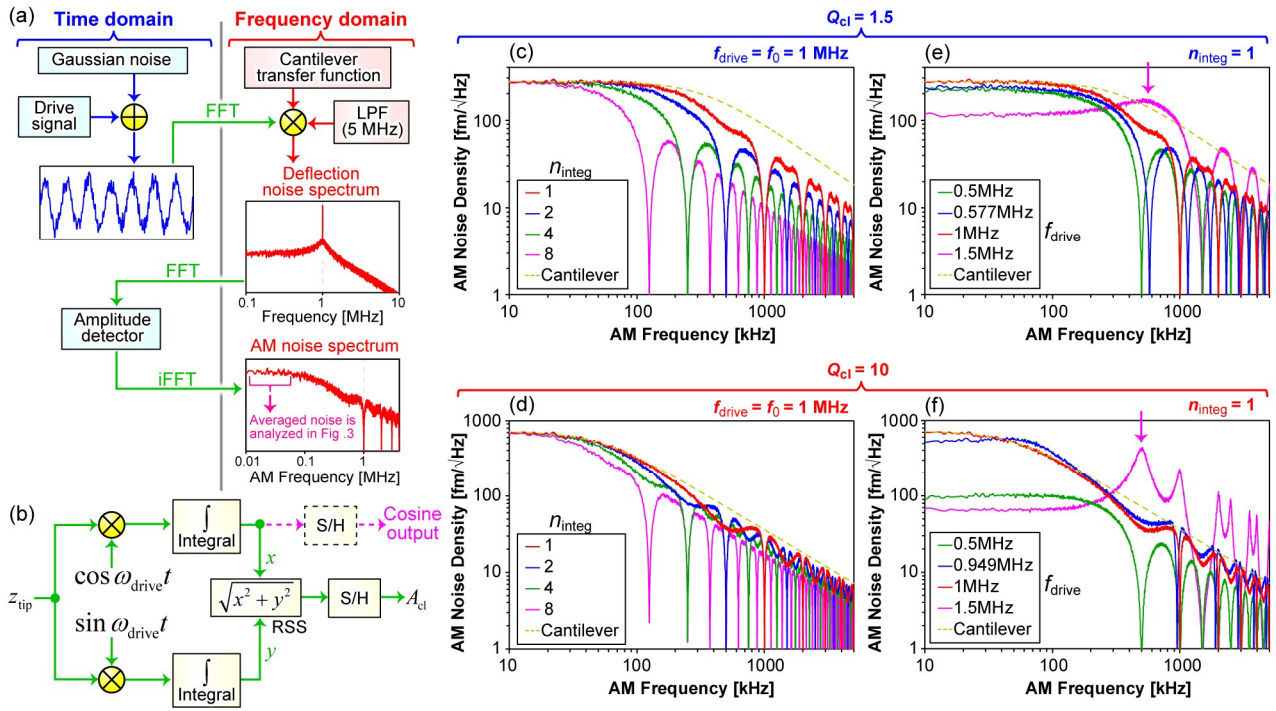


FIG. 2. (a,b) Block diagrams for simulating AM noise spectra in AM-AFM (a) and for the FAB amplitude detector (b). (c-f) AM noise density spectra using FAB, calculated for different n_{integ} values (c,d) and different drive frequencies (e,f) for $Q_{cl} = 1.5$ (c,e) and $Q_{cl} = 10$ (d,f).

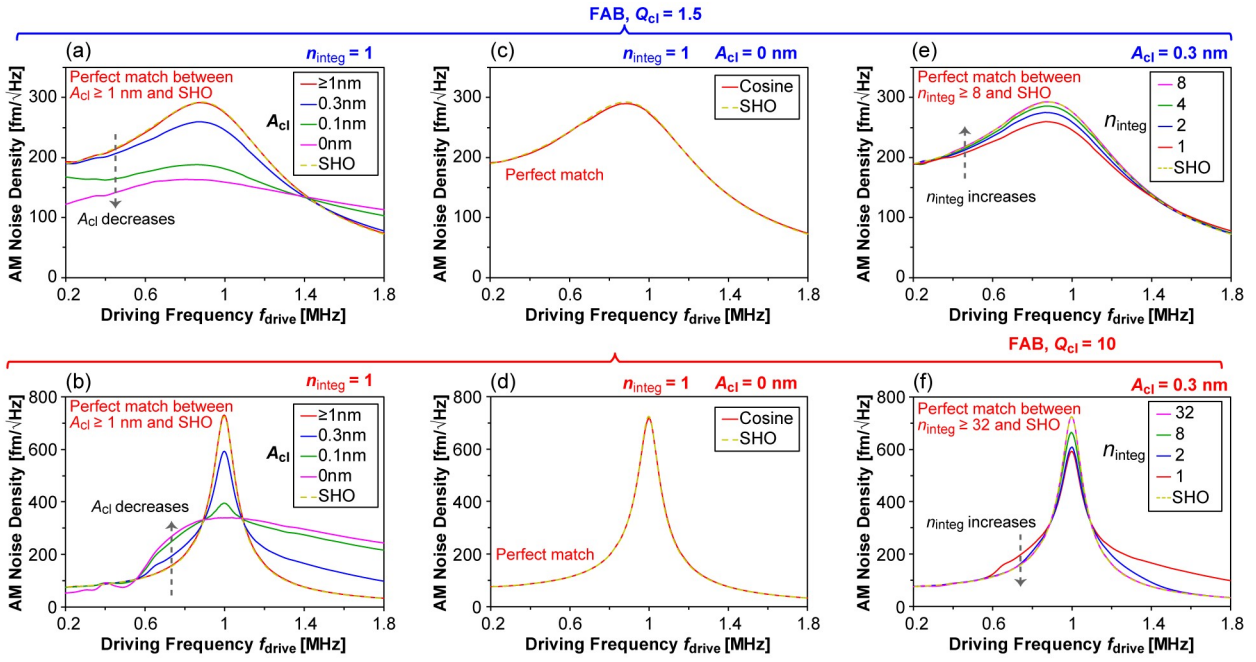


FIG. 3. (a–f) Low-frequency AM noise density as a function of the driving frequency for $Q_{cl} = 1.5$ (a,c,e) and $Q_{cl} = 10$ (b,d,f). The plots include the case of $n_{integ} = 1$ with various A_{cl} (a,b), the case of cosine output (c,d), and the case of $A_{cl} = 0.3$ nm with various n_{integ} (e,f).

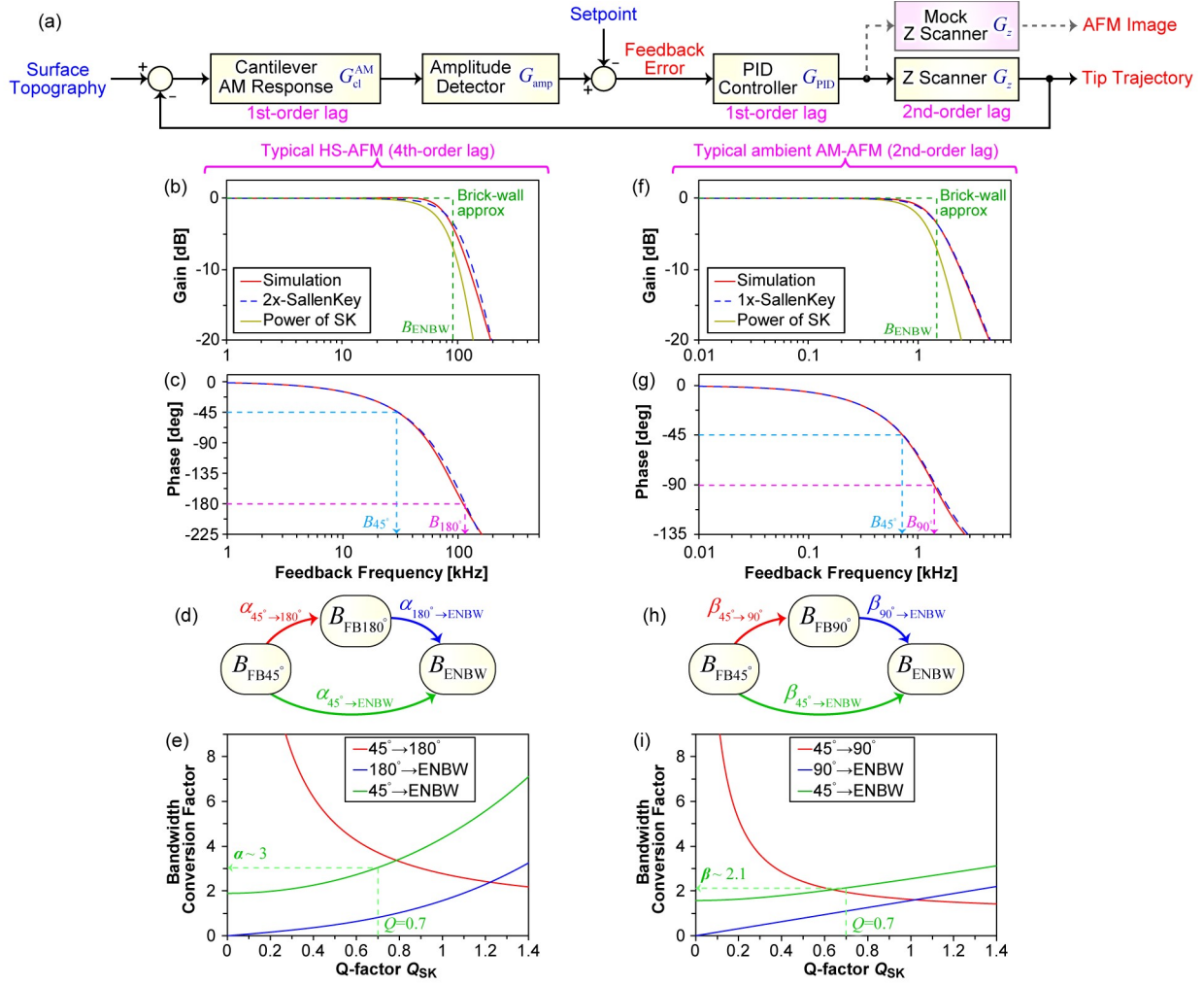


FIG. 4. (a) Block diagram of the AM-AFM feedback closed-loop system designed to control the tip trajectory in order to follow the surface topography. (b,c,f,g) Simulated bode diagram showing the gain (b,f) and phase (c,g) responses of the HS-AFM (b,c) and ambient AM-AFM (d,e) system, with the blue broken lines indicating the fitted 4th and 2nd Sallen-Key approximation, respectively. (d,h) Schematic correlation between B_{FB45° , B_{FB180° , and B_{ENBW} . (e,i) Calculated dependence of the Q-factor on the bandwidth conversion factor.

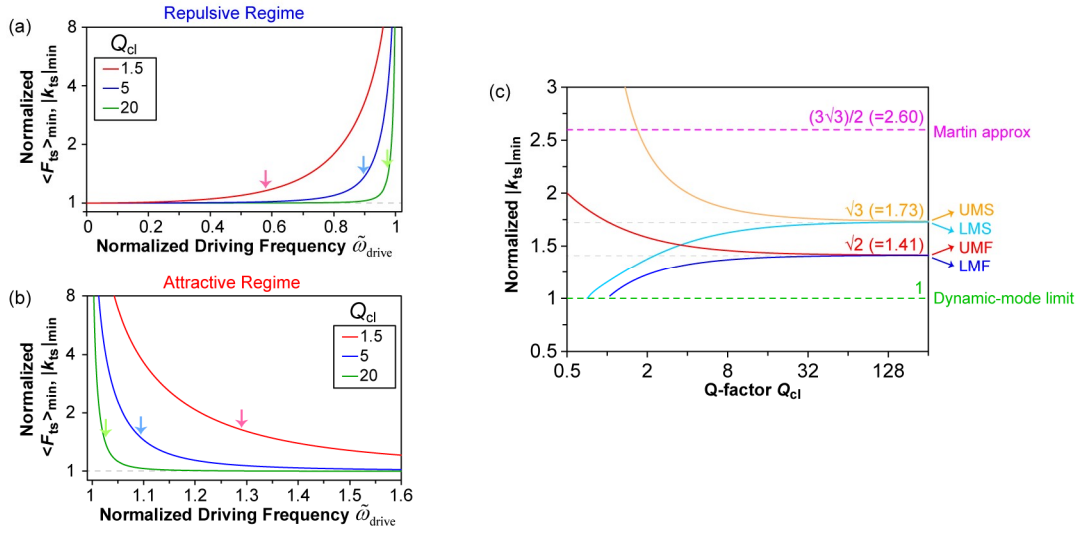


FIG. 5. (a,b) Theoretical driving frequency dependence of minimum detectable force gradient, normalized by the dynamic-mode limit (equivalent to those of minimum detectable force), in the repulsive (a) and attractive (b) regimes at different Q_{cl} values (Eq. (76,77)). The arrows indicate the lower and upper MinForce frequencies. **(c,d)** Dependence of the minimum detectable force gradient on Q_{cl} , normalized by the dynamic-mode limit, shown for the resonance slope frequencies (c) and peak and resonance frequencies (d).

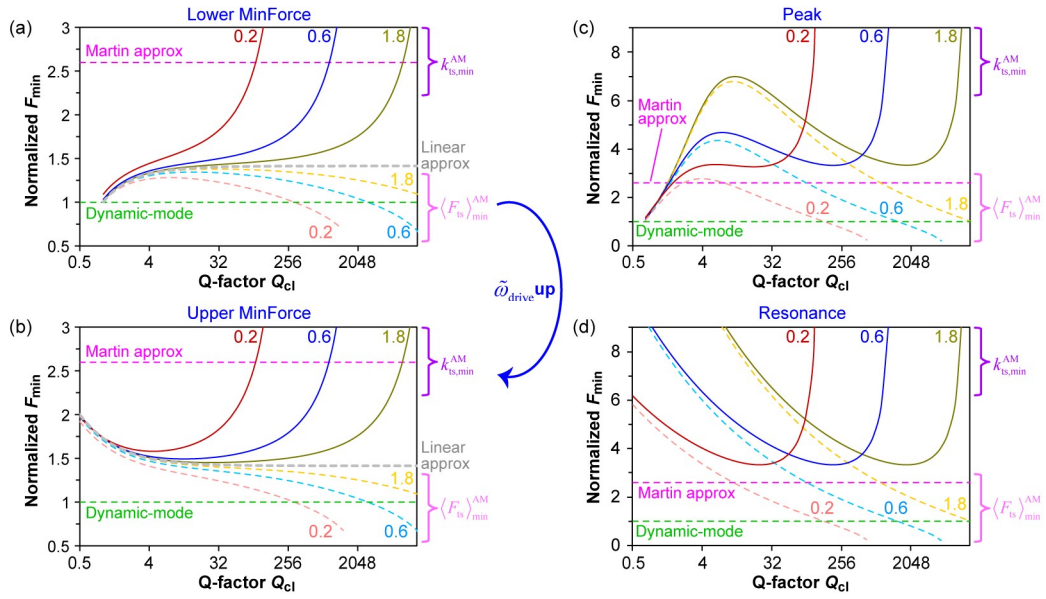


FIG. 6. (a–d) Q_{cl} -dependence of $k_{ts,min}^{AM}$ and $\langle F_{ts} \rangle_{min}^{AM}$, normalized by the dynamic-mode limit for $Ak^{1/2} = 0.2, 0.6,$ and $1.8 \text{ nm} \cdot \sqrt{(\text{N/m})}$ under excitation at the lower MinForce (a), upper MinForce (b), peak (c), and resonance (d) frequencies. The three solid lines at the top represent $k_{ts,min}^{AM}$, while the three broken lines at the bottom represent $\langle F_{ts} \rangle_{min}^{AM}$.

Acknowledgments

This work was supported by PRESTO, Japan Science and Technology Agency (JST) [JPMJPR20E3 and JPMJPR23J2 to K.U.]; and KAKENHI, Japan Society for the Promotion of Science [21K04849 (to K.U.), 20H00327, and 24H00402 (to N.K.)].

Author contributions

K. U. constructed the theories, derived equations, and wrote the manuscript; and N. K. supervised the study.

Data availability

The data that support the findings of this study are available from the corresponding author upon reasonable request.

References

- [1] Y. Martin, C. C. Williams, and H. K. Wickramasinghe, Atomic force microscope-force mapping and profiling on a sub 100-Å scale, *J. Appl. Phys.* **61**, 4723 (1987).
- [2] G. M. McClelland, R. Erlandsson, and S. Chiang, in *Rev. Prog. Quant. Nondestruct. Eval.*, edited by D. O. Thompson, and D. E. Chimenti (Springer, Boston, MA, 1987), pp. 1307.
- [3] R. Garcia and R. Perez, Dynamic atomic force microscopy methods, *Surf. Sci. Rep.* **47**, 197 (2002).
- [4] T. Sulchek, G. G. Yaralioglu, C. F. Quate, and S. C. Minne, Characterization and optimization of scan speed for tapping-mode atomic force microscopy, *Rev. Sci. Instrum.* **73**, 2928 (2002).
- [5] H. Hölscher and U. D. Schwarz, Theory of amplitude modulation atomic force microscopy with and without Q -Control, *Int. J. Non-Linear Mech.* **42**, 608 (2007).
- [6] B. Voigtländer, (Springer, Berlin, 2019), *Atomic Force Microscopy* 2nd ed.
- [7] V. V. Korolkov, A. Summerfield, A. Murphy, D. B. Amabilino, K. Watanabe, T. Taniguchi, and P. H. Beton, Ultra-high resolution imaging of thin films and single strands of polythiophene using atomic force microscopy, *Nat. Commun.* **10**, 1537 (2019).
- [8] A. F. Payam and A. Passian, Imaging beyond the surface region: Probing hidden materials via atomic force microscopy, *Sci. Adv.* **9**, eadg8292 (2023).
- [9] A. F. Payam, D. Martin-Jimenez, and R. Garcia, Force reconstruction from tapping mode

- force microscopy experiments, *Nanotechnology* **26**, 185706 (2015).
- [10] H. Söngen, R. Bechstein, and A. Kühnle, Quantitative atomic force microscopy, *J. Phys. Condens. Matter* **29**, 274001 (2017).
- [11] R. Giridharagopal, L. Q. Flagg, J. S. Harrison, M. E. Ziffer, J. Onorato, C. K. Luscombe, and D. S. Ginger, Electrochemical strain microscopy probes morphology-induced variations in ion uptake and performance in organic electrochemical transistors, *Nat. Mater.* **16**, 737 (2017).
- [12] Y. F. Dufrêne, T. Ando, R. Garcia, D. Alsteens, D. Martinez-Martin, A. Engel, C. Gerber, and D. J. Müller, Imaging modes of atomic force microscopy for application in molecular and cell biology, *Nat. Nanotechnol.* **12**, 295 (2017).
- [13] S. Hoof, N. N. Gosvami, and B. W. Hoogenboom, Enhanced quality factors and force sensitivity by attaching magnetic beads to cantilevers for atomic force microscopy in liquid, *J. Appl. Phys.* **112**, 114324 (2012).
- [14] T. Ando, T. Uchihashi, and T. Fukuma, High-speed atomic force microscopy for nano-visualization of dynamic biomolecular processes, *Prog. Surf. Sci.* **83**, 337 (2008).
- [15] N. Kodera, D. Noshiro, S. K. Dora, T. Mori, J. Habchi, D. Blocquel, A. Gruet, M. Dosnon, E. Salladini, C. Bignon, Y. Fujioka, T. Oda, N. N. Noda, M. Sato, M. Lotti, M. Mizuguchi, S. Longhi, and T. Ando, Structural and dynamics analysis of intrinsically disordered proteins by high-speed atomic force microscopy, *Nat. Nanotechnol.* **16**, 181 (2021).

- [16] T. R. Albrecht, P. Grütter, D. Horne, and D. Rugar, Frequency modulation detection using high- Q cantilevers for enhanced force microscope sensitivity, *J. Appl. Phys.* **69**, 668 (1991).
- [17] T. Fukuma, J. I. Kilpatrick, and S. P. Jarvis, Phase modulation atomic force microscope with true atomic resolution, *Rev. Sci. Instrum.* **77**, 123703 (2006).
- [18] N. Kobayashi, Y. J. Li, Y. Naitoh, M. Kageshima, and Y. Sugawara, High force sensitivity in Q -controlled phase-modulation atomic force microscopy, *Appl. Phys. Lett.* **97**, 011906 (2010).
- [19] N. Kobayashi, Y. J. Li, Y. Naitoh, M. Kageshima, and Y. Sugawara, High-sensitivity force detection by phase-modulation atomic force microscopy, *Jpn. J. Appl. Phys., Part 2* **45**, L793 (2006).
- [20] F. He, J. Liu, and K. D. Zhu, Optomechanical atomic force microscope, *Nanotechnology* **32**, 085505 (2021).
- [21] H. Hida, M. Shikida, K. Fukuzawa, S. Murakami, K. Sato, K. Asaumi, Y. Iriye, and K. Sato, Fabrication of a quartz tuning-fork probe with a sharp tip for AFM systems, *Sensor. Actuat. A-Phys.* **148**, 311 (2008).
- [22] K. Hirata, T. Igarashi, K. Suzuki, K. Miyazawa, and T. Fukuma, Wideband Magnetic Excitation System for Atomic Force Microscopy Cantilevers with Megahertz-Order Resonance Frequency, *Sci. Rep.* **10**, 9133 (2020).
- [23] J. Kim, B. Sung, B. I. Kim, and W. Jhe, Optimization of force sensitivity in Q -controlled

- amplitude-modulation atomic force microscopy, *J. Appl. Phys.* **114**, 054302 (2013).
- [24] E. Wutscher and F. J. Giessibl, Atomic force microscopy at ambient and liquid conditions with stiff sensors and small amplitudes, *Rev. Sci. Instrum.* **82**, 093703 (2011).
- [25] K. Umeda, K. Kamoshita, and N. Kodera, Quantitative Formulation of Frequency-Dependent Average Force in AM-AFM, arXiv, 2407.18748 (2024).
- [26] K. Umeda and N. Kodera, Guidelines for Fast and Nondestructive Imaging in AM-AFM, arXiv, 2411.16317 (2024).
- [27] A. J. Katan, M. H. van Es, and T. H. Oosterkamp, Quantitative force versus distance measurements in amplitude modulation AFM: a novel force inversion technique, *Nanotechnology* **20**, 165703 (2009).
- [28] A. Raman, X. Xu, C. Carrasco, P. J. de Pablo, and J. Gomez-Herrero, Unmasking imaging forces on soft biological samples in liquids when using dynamic atomic force microscopy: A case study on viral capsids, *Biophys. J.* **95**, 2520 (2008).
- [29] V. Vahdat and R. W. Carpick, Practical Method to Limit Tip-Sample Contact Stress and Prevent Wear in Amplitude Modulation Atomic Force Microscopy, *ACS Nano* **7**, 9836 (2013).
- [30] A. P. Nievergelt, N. Banterle, S. H. Andany, P. Gonczy, and G. E. Fantner, High-speed photothermal off-resonance atomic force microscopy reveals assembly routes of centriolar scaffold protein SAS-6, *Nat. Nanotechnol.* **13**, 696 (2018).

- [31] Tim J. Sobering, SDE consulting, Equivalent Noise Bandwidth, Tech note, <https://www.k-state.edu/edl/docs/pubs/technical-resources/Technote1.pdf> (Accessed Aug, 2024)
- [32] T. Fukuma, M. Kimura, K. Kobayashi, K. Matsushige, and H. Yamada, Development of low noise cantilever deflection sensor for multienvironment frequency-modulation atomic force microscopy, *Rev. Sci. Instrum.* **76**, 053704 (2005).
- [33] T. Fukuma and S. P. Jarvis, Development of liquid-environment frequency modulation atomic force microscope with low noise deflection sensor for cantilevers of various dimensions, *Rev. Sci. Instrum.* **77**, 043701 (2006).
- [34] J. D. Adams, B. W. Erickson, J. Grossenbacher, J. Brugger, A. Nievergelt, and G. E. Fantner, Harnessing the damping properties of materials for high-speed atomic force microscopy, *Nat. Nanotechnol.* **11**, 147 (2016).
- [35] F. Sumbul, N. Hassanpour, J. Rodriguez-Ramos, and F. Rico, One-Step Calibration of AFM in Liquid, *Front. Phys.* **8**, 301 (2020).
- [36] C. Valotteau, F. Sumbul, and F. Rico, High-speed force spectroscopy: microsecond force measurements using ultrashort cantilevers, *Biophys. Rev.* **11**, 689 (2019).
- [37] K. Kobayashi, H. Yamada, and K. Matsushige, Frequency noise in frequency modulation atomic force microscopy, *Rev. Sci. Instrum.* **80**, 043708 (2009).
- [38] K. Kobayashi, H. Yamada, and K. Matsushige, Reduction of frequency noise and frequency shift by phase shifting elements in frequency modulation atomic force microscopy, *Rev. Sci.*

Instrum. **82**, 033702 (2011).

- [39] K. Umeda, C. Okamoto, M. Shimizu, S. Watanabe, T. Ando, and N. Kodera, Architecture of zero-latency ultrafast amplitude detector for high-speed atomic force microscopy, *Appl. Phys. Lett.* **119**, 181602 (2021).